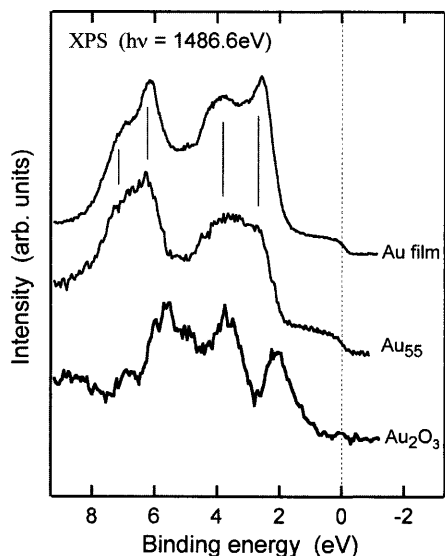


## REPORTS



**Fig. 4.** XPS valence band spectra of naked Au<sub>55</sub> clusters supported on silicon oxide, together with the corresponding spectra measured from an Au film and the Au<sub>2</sub>O<sub>3</sub> compound (6), respectively.

caused by size-induced modifications in the electronic structure. Rather, the closing of the second atomic shell is a more likely origin for the increased chemical stability. "Chemical selection," which avoids having an arbitrary number of atoms in a particle during the formation of phosphine-based Au clusters (Au<sub>13</sub>, Au<sub>55</sub>, Au<sub>147</sub>, etc.), might itself result in oxidation resistance. On the other hand, the chemical stability of Au<sub>55</sub> clusters might also be influenced by a high density of defects in the supporting material caused by the initial oxygen plasma treatment to remove the ligand shell. Defects in the support are known to modify the reactivity of Au clusters as compared to that of clusters on perfect substrates (7).

The observed stability against oxidation does not reflect a general property of ultrafine Au particles for particle diameters below a certain threshold. Rather, a nonmonotoneous size dependence was found with a pronounced minimum of reactivity for a cluster size of 1.4 nm. Interestingly enough, such a minimum of reactivity with atomic oxygen coincides with the existence of a pronounced maximum of catalytic efficiency for oxidation of CO to CO<sub>2</sub> (8). Thus, we may speculate that Au<sub>55</sub> clusters also exhibit unusual catalytic properties, such as in the oxidation of CO, because the catalyzing clusters will not be affected by the presence of atomic oxygen during the catalytic reaction.

### References and Notes

1. M. Peuckert, F. P. Coenen, H. P. Bonzel, *Surf. Sci.* **141**, 515 (1984).
2. D. H. Parker, B. E. Koel, *J. Vac. Sci. Technol. A* **8**, 2585 (1990).
3. D. D. Eley, P. B. Moore, *Surf. Sci.* **76**, L599 (1978).

4. J. J. Pireau, M. Liehr, P. A. Thiry, J. P. Delrue, R. Caudano, *Surf. Sci.* **141**, 221 (1984).
5. H. Ron, I. Rubinstein, *Langmuir* **10**, 4566 (1994).
6. B. Koslowski et al., *Surf. Sci.* **475**, 1 (2001).
7. U. Heiz, W.-D. Schneider, *J. Phys. D Appl. Phys.* **33**, R85 (2000).
8. M. Valden, X. Lai, D. W. Goodman, *Science* **281**, 1647 (1998).
9. M. Haruta, *Catal. Today* **36**, 153 (1997).
10. C. R. Henry, *Surf. Sci. Rep.* **31**, 231 (1998).
11. J. P. Spatz et al., *J. Lumin.* **76/77**, 168 (1998).
12. All photoemission experiments were carried out in a FISON ESCALAB-210 electron spectrometer, allowing in situ preparation and analysis by means of monochromatized Al-K $\alpha$  radiation (photon energy  $h\nu = 1486.6$  eV).
13. G. Schmid *Inorg. Synth.* **7**, 214 (1990).
14. Although other small gold clusters (such as Au<sub>13</sub>) have been reported, only Au<sub>55</sub> appears to be readily synthesized in sufficient yield for studies such as these.
15. G. Radu, U. Memmert, U. Hartmann, *Proc. Spring Meet. German Phys. Soc. (Hamburg) Verhandl. DPG (VI)* **36**, 393 (2001).
16. The thickness of the surface oxide can be estimated within an analysis using Doniach-Sunjic line shapes (20) to model the different contributions to the spectra (27) and applying standard formulas for angle-resolved photoemission (22). Taking estimated mean free path values for the Au-4f photoelectrons

of 2.0 and 3.1 nm (23) and known density values of 19.3 g cm<sup>-3</sup> and 11 g cm<sup>-3</sup> for the pure Au metal and the Au<sub>2</sub>O<sub>3</sub> compound, respectively, a thickness of 2.9 nm can be extracted for the oxide layer from Fig. 3A, in agreement with previous experiments on ex situ plasma-oxidized Au films (6).

17. The nanoparticle is divided into a large number of identical cells, each contributing to the photoelectron current an intensity that is affected by the attenuation in cells being closer to the surface according to the mean free path of the corresponding material within these cells (Au and Au<sub>2</sub>O<sub>3</sub>).
18. R. E. Leuchtner, A. C. Harms, J. A. W. Castleman, *J. Chem. Phys.* **91**, 2753 (1989).
19. H.-G. Boyen et al., *Phys. Rev. Lett.* **87**, 276401 (2001).
20. S. Doniach, M. Sunjic, *J. Phys. C* **3**, 385 (1970).
21. G. K. Wertheim, S. B. DiCenzo, *J. Electron. Spectrosc.* **37**, 57 (1985).
22. B. L. Henke, *Phys. Rev. A* **6**, 94 (1972).
23. M. P. Seah, W. A. Dench, *Surf. Interface Anal.* **1**, 2 (1979).
24. Financial support by the Bundesministerium für Bildung und Forschung, the Deutsche Forschungsgemeinschaft within SFB 569 and SPP 1072, the Swiss National Science Foundation, and the National Center of Competence in Research "Nanoscale Science" is gratefully acknowledged.

17 July 2002; accepted 25 July 2002

# Nanoparticles with Raman Spectroscopic Fingerprints for DNA and RNA Detection

YunWei Charles Cao, Rongchao Jin, Chad A. Mirkin\*

Multiplexed detection of oligonucleotide targets has been performed with gold nanoparticle probes labeled with oligonucleotides and Raman-active dyes. The gold nanoparticles facilitate the formation of a silver coating that acts as a surface-enhanced Raman scattering promoter for the dye-labeled particles that have been captured by target molecules and an underlying chip in microarray format. The strategy provides the high-sensitivity and high-selectivity attributes of gray-scale scanometric detection but adds multiplexing and ratioing capabilities because a very large number of probes can be designed based on the concept of using a Raman tag as a narrow-band spectroscopic fingerprint. Six dissimilar DNA targets with six Raman-labeled nanoparticle probes were distinguished, as well as two RNA targets with single nucleotide polymorphisms. The current unoptimized detection limit of this method is 20 femtomolar.

A highly sensitive and selective detection format for DNA relies on oligonucleotide-functionalized nanoparticles as probes, a particle-initiated Ag developing technique for signal enhancement, and a flatbed scanner for optical readout (1). The documented detection limit for this "scanometric DNA detection" format is 50 fM, (1) and the utility of the system has been demonstrated with short synthetic strands, polymerase chain reaction products, and genomic DNA targets (2, 3). However, a limitation of this approach is that

it is inherently a one-color system based on gray scale. The flexibility and applicability of all DNA-detection systems benefit from access to multiple types of labels with addressable and individually discernable labeling information. In the case of fluorescence, multiple fluorophores, including quantum dots, can be used to prepare encoded structures with optical signatures that depend on the types of fluorophores used and their signal ratio within the probes (4, 5). These approaches typically use micrometer-sized probes to obtain encoded structures with the appropriate signal intensities and uniformities. In the case of molecular fluorophores, overlapping spectral features and nonuniform fluorophore photobleaching rates lead to several potential complications (4, 6, 7).

Department of Chemistry and Institute for Nanotechnology, Northwestern University, 2145 Sheridan Road, Evanston, IL 60208, USA.

\*To whom correspondence should be addressed: camirkin@chem.northwestern.edu

## REPORTS

Here, we show that nanoparticles functionalized with oligonucleotides and Raman labels, coupled with surface-enhanced Raman scattering (SERS) spectroscopy, can be used to perform multiplexed detection of oligonucleotide targets (Scheme 1). Although oligonucleotides can be directly detected by SERS on aggregated particles (7, 8), the structural similarities of oligonucleotides with different sequences result in spectra that are difficult to distinguish. Therefore, researchers often use different Raman dyes to label different oligonucleotides to distinguish oligonucleotide sequences (9, 10). To realize the benefits of high-sensitivity and high-selectivity detection coupled with multiple labeling capabilities, we designed nanoparticle probes that can be used for DNA (or RNA) detection (Scheme 1). These probes consist of 13-nm-diameter Au particles functionalized with Raman dye-labeled oligonucleotides. The Raman spectroscopic fingerprint, which can be designed through choice of Raman label, can be identified after Ag enhancing by scanning Raman spectroscopy (Scheme 1). Because the SERS-active substrate in this strategy is generated immediately before the detection event, a large and reproducible Raman scattering response can be obtained.

In a typical experiment for DNA detection, a three-component sandwich assay is used in microarray format (Scheme 1). Au nanoparticles ( $13 \pm 2$  nm in diameter) modified with Cy3-labeled, alkylthiol-capped oligonucleotide strands were used as probes to monitor the presence of specific target DNA strands (11). On average, there are about 110 oligonucleotide strands on each 13-nm Au nanoparticle (12). The Cy3 group was chosen as a Raman label because of its large Raman cross section (13). A chip spotted with the appropriate 15-nucleotide capture strands was coated with a 0.6 M NaCl phosphate-buffered saline (PBS) buffer solution (10 mM of phosphate, pH 7) containing a 30-nucleotide target sequence (100 pM) in a humidity chamber at room temperature. After 4 hours, the chip was washed four times with 0.6 M NaCl PBS buffer solution to remove nonspecifically bound target. Then, the chip was treated with a 0.6 M NaCl PBS solution of nanoparticle probes (2 nM) for 1.5 hours to effect hybridization with the overhanging region of the target sequence (Scheme 1). The chip was then washed with 0.6 M NaNO<sub>3</sub> PBS buffer solution to remove chloride ions and nonspecifically bound nanoparticle probes. The chip was immediately treated with a Ag enhancement solution (Ted Pella, Inc., Redding, California) for 8 min, rinsed with Nanopure water, and dried with a microarray centrifuge (2000g). The chip, which exhibits gray spots visible to the naked eye, could be imaged with a flatbed scanner (Expression 1600, Epson America, Torrance, California) (Fig. 1B) (1–3). The spots also were studied by a Raman spectrometer coupled with a

fiber-optic probe with a 0.65-numerical aperture microscope objective (25- $\mu$ m laser beam) in a 0.3 M NaCl PBS buffer solution (Fig. 1C), and each of them shows a consistent and strong Raman response at 1192  $\text{cm}^{-1}$  (Fig. 1D) (Solution Raman 633 spectrometer from Concurrent Analytical, Inc., Waimanalo, Hawaii; 30 mW He-Ne laser).

Before Ag enhancing, the nanoparticle probes were invisible to the naked eye, and no Raman scattering signal was detectable (Fig. 1A). This is due to a lack of electromagnetic-field enhancement for the undeveloped nanoparticles (13 nm in diameter) in this state (7, 14, 15). Others have shown that closely spaced Au nanoparticles can give SERS enhancement (16, 17), but for DNA detection at technologically relevant target concentrations (<1 nM), nanopar-

ticle spacings are too large to yield such effects. After Ag enhancing, the Ag particles can grow around the Cy3-labeled nanoparticle probes, leading to large Raman scattering enhancements. Typically, the spectra include both sharp Raman lines ( $\sim 15$  to 30  $\text{cm}^{-1}$  in spectral width) and a concomitant broad underlying continuum, as noted by Brus *et al.* in their studies of rhodamine 6G molecules on Ag particles (18). The Raman scattering signals arise almost exclusively from the Cy3 dye molecules immobilized on the particles; we do not observe signals from other species such as the oligonucleotides, solvent molecules, and the succinimidyl 4-(*p*-maleimidophenyl)butyrate on the glass surface. The Raman scattering frequency for each Raman line remains constant from experiment to

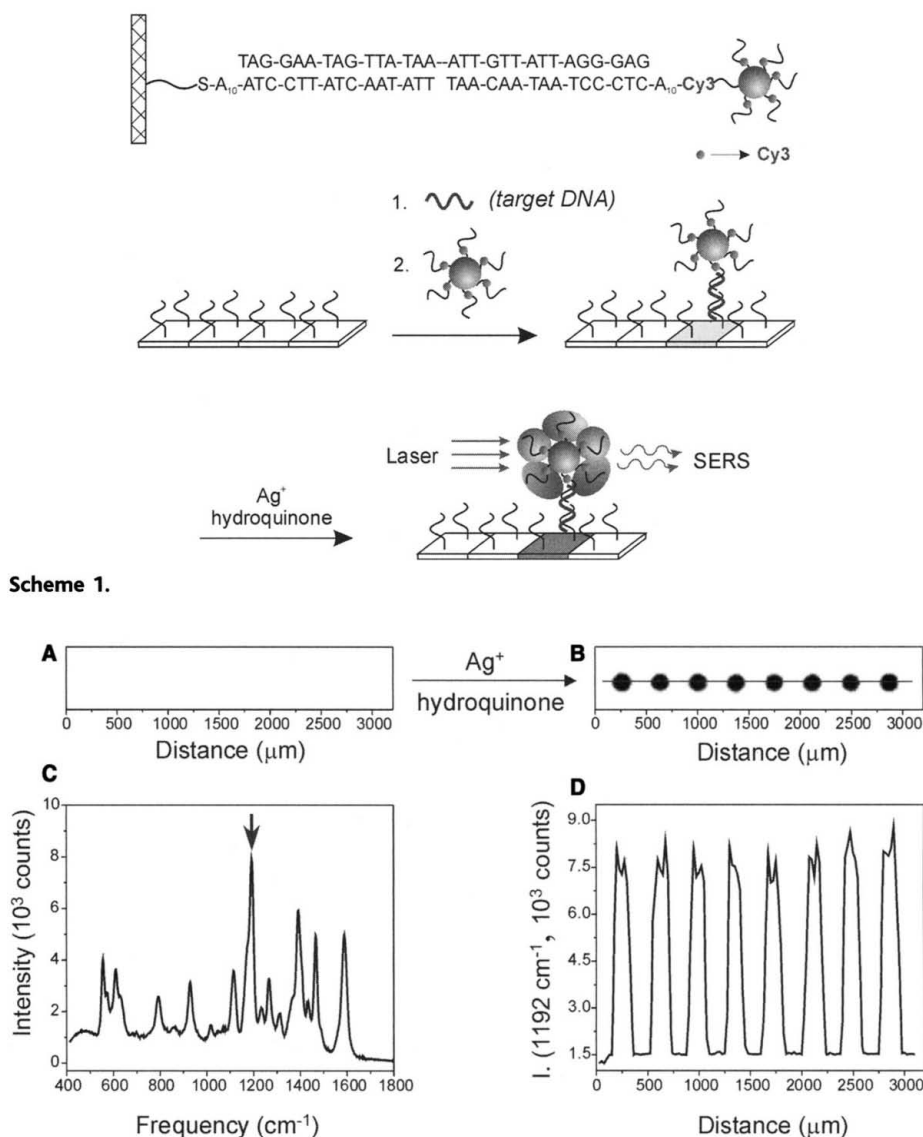
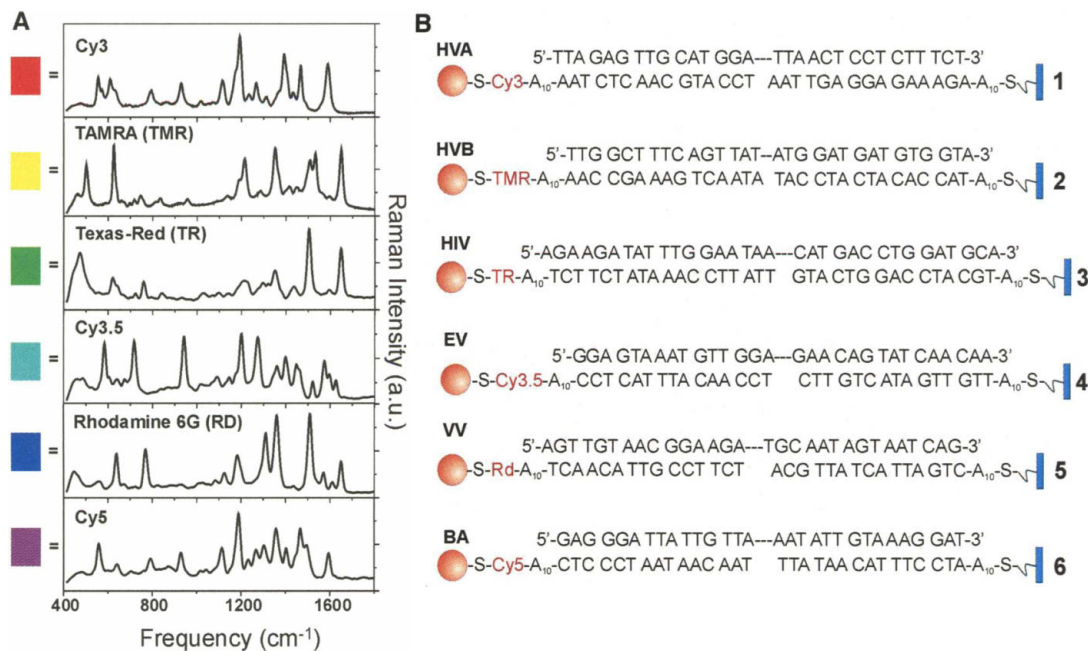


**Fig. 2. (A)** The Raman spectra of six dye-labeled nanoparticle probes after Ag enhancing on a chip (after background subtraction). Each dye correlates with a different color in our labeling scheme (see rectangular boxes). TAMRA, tetramethyl rhodamine. **(B)** Six DNA sandwich assays with corresponding target analysis systems. A<sub>10</sub> is an oligonucleotide tether with 10 adenosine units.



experiment, deviating by less than 2 cm<sup>-1</sup>. These consistent SERS signals from the Cy3-labeled nanoparticle probes allow us to use the Raman spectrum of Cy3 as a spectroscopic fingerprint to monitor the presence of a specific target oligonucleotide strand.

Dyes other than Cy3 can be used to create a large number of probes with distinct and measurable SERS signals for multiplexed detection. To demonstrate this point, we selected six commercially available dyes with distinct Raman spectra that can be incorporated into oligonucleotides through standard automated DNA syntheses. Six types of Raman-labeled and oligonucleotide-modified Au nanoparticle probes were prepared with sequences that were respectively complementary to statistically unique 30- to 36-nucleotide sequences for (A) hepatitis A virus Vall7 polyprotein gene (HVA), (B) hepatitis B virus surface antigen gene (HVB), (C) human immunodeficiency virus (HIV), (D) Ebola virus (EV), (E) variola virus (smallpox, VV), and (F) *Bacillus anthracis* (BA) protective antigen gene (Fig. 2) (11).

Eight separate tests were carried out to evaluate the selectivity of the system and our ability to determine the number and types of strands in solutions containing mixtures of the different targets (Figs. 2 and 3). The concentrations of the target strands were kept constant for all of these experiments (100 pM each), and the hybridization conditions were as described above. In the first test (Fig. 3, row 1), all spots show the same intense gray color associated with Ag deposition. However, they can be differentiated simply by using the Raman scanning method. Once the spectroscopic fingerprint of the Ag-containing

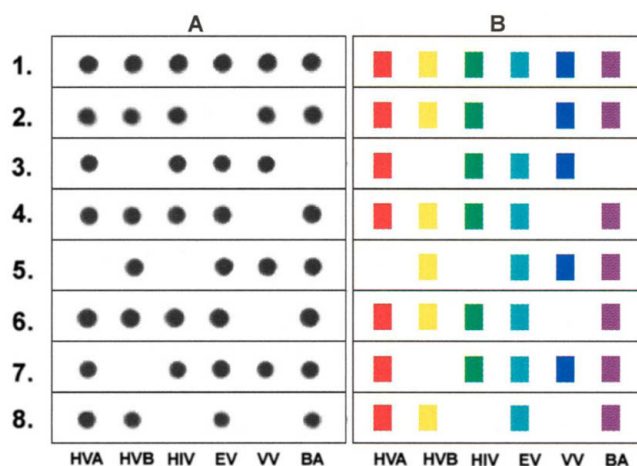


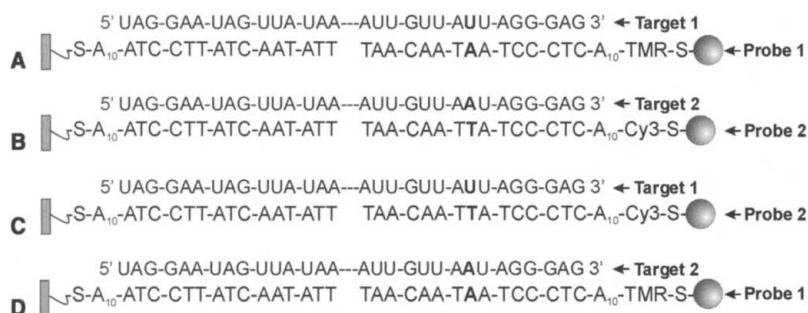
**Fig. 3. (A)** Flatbed scanner images of Ag-enhanced microarrays and **(B)** corresponding Raman spectra. The colored boxes correlate with the color-coded Raman spectra in Fig. 2. No false-positives or false-negatives were observed.

spot has been determined, the correct Raman label and, therefore, target sequence can be identified. To simplify the analysis, we assigned a color (rectangular box) to each Raman-labeled probe (Fig. 2A and Fig. 3B). In the first test (Fig. 3A), all six targets were present, and all showed strong gray-scale values when measured by means of the flatbed scanner as well as the expected Raman fingerprints. In the next seven tests, we systematically removed one or more of the targets to evaluate the suitability of this method for multiplexing. With the single-color gray-scale method one cannot determine if any cross-hybridization has occurred. However, with this “multiple color” scanning Raman method, one can carefully study the SERS spectra of each spot to determine which labels make up each spot. For the experiments described in Fig. 3, where the sequences are very dissimilar, we found that other than the expected spectroscopic probe signature for

each target, there were virtually no other detectable Raman lines, indicating no cross-hybridization between different targets and probes. The SERS signal was obtained only from areas of the substrate where the Raman dye-labeled Au particles have initiated Ag formation. Therefore, this “multiple color” scanning Raman detection method does not record background signal due to Ag deposition where Au particles do not exist. This is not the case for the previous gray-scale scanometric approach, especially at ultralow target concentrations (≤50 fM) (1–3). The current unoptimized detection limit of this Raman scanning method is 20 fM (11).

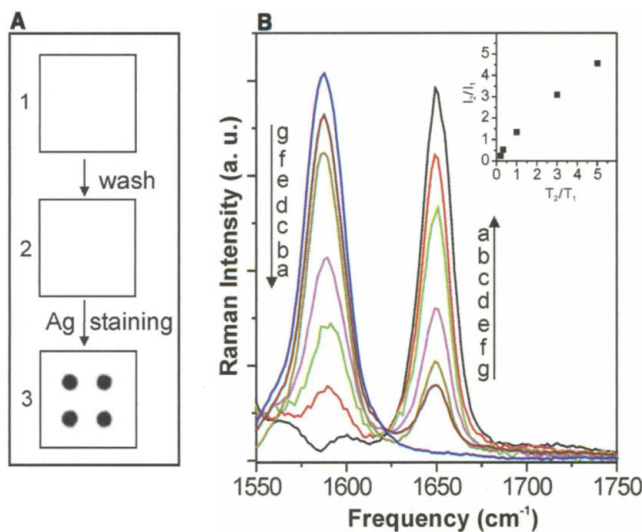
One would like to be able to use such detection systems to differentiate single nucleotide polymorphisms (SNPs), and in the case of gene expression studies, one would like access to RNA detection with single-spot signal ratioing capabilities. Nanoparticle probes heavily functionalized with oligonu-

REPORTS



Scheme 2.

**Fig. 4. (A)** Typical flatbed scanner images of microarrays hybridized with nanoparticles (1) before and (2) after stringency wash but before Ag enhancing, and (3) after Ag enhancing. **(B)** Raman spectra (from 1550 to 1750  $\text{cm}^{-1}$ ) from the stained spots at different ratios of target 1 and target 2: (a) 1:0; (b) 5:1; (c) 3:1; (d) 1:1; (e) 1:3; (f) 1:5; (g) 0:1. The full Raman spectra from 400 to 1800  $\text{cm}^{-1}$  are shown in the supporting text. (Inset) Profile of Raman intensity ratio ( $I_2/I_1$ ) versus target ratio ( $T_2/T_1$ ), where  $I_1$  is the Raman intensity at 1650  $\text{cm}^{-1}$  (from probe 1, TMR labeled);  $I_2$  is the Raman intensity at 1588  $\text{cm}^{-1}$  (from probe 2, Cy3 labeled).



cleotides exhibit extraordinarily sharp thermally induced denaturation transitions that lead to substantially higher selectivity than conventional molecular fluorophore probes and microscopic bead probes in DNA detection (1, 19). However, thus far the behavior of these probes in the context of RNA detection has not been explored. To further test the selectivity of this Raman-based system and its ability to identify SNP targets, we chose two RNA targets that can bind to the same capture-strand DNA but have a single-base mutation in the probe-binding regions (target 1:  $T_1$ , normal; target 2:  $T_2$ , single-base difference) (Scheme 2). Therefore, two DNA-functionalized nanoparticle probes (probe 1:  $P_1$ , probe 2:  $P_2$ ), which differ in sequence and Raman label, are required to differentiate these two RNA target strands (Scheme 2). Seven separate tests were performed to show not only how the two targets ( $T_1$  and  $T_2$ ) can be differentiated, but also how mixtures of the two targets can be analyzed in semiquantitative fashion.

In each of these tests, a slide was treated with a 0.3 M NaCl PBS buffer solution containing  $T_1$  and  $T_2$  in different ratios (total concentration = 1 nM) in a humidity chamber. After 2 hours, the chip was washed with a 0.3

M NaCl PBS buffer to remove nonspecifically bound target. Then, the chip was treated with nanoparticle probes ( $P_1$  and  $P_2$  at 1:1 ratio, 2 nM total concentration) for 1.5 hours to effect hybridization with the overhanging region of the target sequences (Scheme 2). The chip was washed with 0.3 M  $\text{NaNO}_3$  PBS buffer solution to remove chloride ions and nonspecifically bound nanoparticle probes. There are four possible hybridization modes, namely,  $T_1:P_1$ ,  $T_2:P_2$ ,  $T_1:P_2$ , and  $T_2:P_1$  (Scheme 2). When the chip was developed by Ag enhancing without a previous stringency wash, the Raman measurements on the gray spots, which correspond to different solution target ratios, yielded nearly identical spectra in all seven experiments; these spectra also are almost identical to those obtained for a sample containing a 1:1 ratio of probe 1 and probe 2 (11). These data show that probe 1 and probe 2 are bound to the spots on the chip in equal amounts, regardless of the target composition on the spot.

To identify the target composition on the spots, one must apply a salt- or temperature-based stringency wash (1, 19). Accordingly, we used a salt stringency wash (8 mM NaCl PBS buffer) to selectively denature the imperfect duplexes ( $T_1:P_2$  and/or  $T_2:P_1$ ) (Scheme 2, C and D) but not the duplexes

formed from the perfectly complementary oligonucleotides ( $T_1:P_1$  and/or  $T_2:P_2$ ) (Scheme 2, A and B). After stringency wash and subsequent Ag staining, the Raman analysis of the gray spots can be used to readily identify the target composition on the spots by their spectral fingerprints. In tests where only pure RNA target 1 or 2 is present, only signals for probe 1 or 2, respectively, were observed (compare Fig. 4B, “a” and “g”) (11). In the case of mixtures, signals for both probes ( $I_1$  at 1650  $\text{cm}^{-1}$  from probe 1 and  $I_2$  at 1588  $\text{cm}^{-1}$  from probe 2) were detected, and the intensity ratios are proportional to the ratios of the two targets in each experiment (Fig. 4B, inset).

Compared with fluorescence-based chip detection, this nanoparticle-based methodology offers several advantages. The ratio of Raman intensities can be extracted from a single Raman spectrum with single-laser excitation. Second, the number of available Raman dyes is much greater than the number of available and discernable fluorescent dyes (7, 9). Indeed, a Raman dye can be either fluorescent or nonfluorescent, but a minor chemical modification of a dye molecule can lead to a new dye with a different Raman spectrum even though the two dyes exhibit virtually indistinguishable fluorescence spectra (7). Therefore, this fingerprinting method offers potentially greater flexibility, a larger pool of available and nonoverlapping probes, and higher multiplexing capabilities than conventional fluorescence-based detection approaches. Finally, the method incorporates all of the previous advantages of Au-nanoparticle based detection, including several orders of magnitude higher sensitivity and many orders of magnitude higher selectivity than the analogous molecular fluorescence-based approach (1, 19). When considered with previous demonstrations of the unique properties of nanoparticle probes (1–4, 19–27), a strong argument is being made for nanoparticles as the next-generation labeling technology for biodiagnostic research.

References and Notes

1. T. A. Taton, C. A. Mirkin, R. L. Letsinger, *Science* **289**, 1757 (2000).
2. See [www.nanosphere-inc.com](http://www.nanosphere-inc.com); unpublished work has improved sensitivity to 100 aM.
3. C. A. Mirkin, American Association for Clinical Chemistry Meeting, San Diego, CA, 2001.
4. M. Han, X. Gao, J. Z. Su, S. Nie, *Nature Biotechnol.* **19**, 631 (2001).
5. D. R. Walt, *Science* **287**, 451 (2000).
6. G. Gibson, S. V. Muse, *A Primer of Genome Science* (Sinauer, Sunderland, MA, 2002).
7. K. Kneipp, H. Kneipp, I. Itzkan, R. R. Dasari, M. S. Feld, *Chem. Rev.* **99**, 2957 (1999).
8. L. A. Gearheart, H. J. Ploehn, C. J. Murphy, *J. Phys. Chem. B.* **105**, 12609 (2001).
9. D. Graham, B. J. Mallinder, W. E. Smith, *Angew. Chem. Int. Ed.* **39**, 1061 (2000).
10. N. R. Isola, D. L. Stokes, T. Vo-Dinh, *Anal. Chem.* **70**, 1352 (1998).

11. Materials and methods are available as supporting material on *Science Online*.
12. L. M. Demers *et al.*, *Anal. Chem.* **72**, 5535 (2000).
13. R. L. McCreery, *Raman Spectroscopy for Chemical Analysis* (Wiley, New York, 2000).
14. G. C. Schatz, R. P. Van Duyne, in *Handbook of Vibrational Spectroscopy*, J. M. Chalmers, P. R. Griffiths, Eds. (Wiley, New York, 2002), pp. 759–774.
15. A. Campion, P. Kambhampati, *Chem. Soc. Rev.* **27**, 241 (1998).
16. S. R. Emory, S. Nie, *J. Phys. Chem. B* **102**, 493 (1998).
17. M. D. Musick, C. D. Keating, M. H. Keefe, M. J. Natan, *Chem. Mater.* **9**, 1499 (1997).
18. A. M. Michaels, M. Nirmal, L. E. Brus, *J. Am. Chem. Soc.* **121**, 9932 (1999).
19. S. J. Park, T. A. Taton, C. A. Mirkin, *Science* **295**, 1503 (2002).
20. M. Bruchez Jr., M. Moronne, P. Gin, S. Weiss, A. P. Alivisatos, *Science* **281**, 2013 (1998).
21. W. C. W. Chan, S. Nie, *Science* **281**, 2016 (1998).
22. L. He *et al.*, *J. Am. Chem. Soc.* **122**, 9071 (2000).
23. I. Willner, F. Patolsky, J. Wasserman, *Angew. Chem. Int. Ed.* **40**, 2261 (2001).
24. H. Mattoussi *et al.*, *J. Am. Chem. Soc.* **122**, 12142 (2000).
25. S. Pathak, S. K. Choi, N. Arnhem, M. E. Thompson, *J. Am. Chem. Soc.* **123**, 4103 (2001).
26. Y. Cui, Q. Wei, H. Park, C. M. Lieber, *Science* **293**, 1289 (2001).
27. C. M. Niemeyer, *Angew. Chem. Int. Ed.* **40**, 4128 (2001).

28. We acknowledge R. L. Letsinger and L. G. Zhang for helpful discussions. C.A.M. acknowledges the Air Force Office of Scientific Research (AFOSR), the Defense Advanced Research Projects Agency (DARPA), and the NSF for support of this research. R.J. is grateful for the support of the American Chemical Society Cognis Fellowship in Colloid and Surface Chemistry.

**Supporting Online Material**

[www.sciencemag.org/cgi/content/full/297/5586/1536/DC1](http://www.sciencemag.org/cgi/content/full/297/5586/1536/DC1)  
Materials and Methods  
Schemes S1 and S2  
Figs. S1 to S3

12 June 2002; accepted 31 July 2002

## Fluidity of Bound Hydration Layers

Uri Raviv<sup>1</sup> and Jacob Klein<sup>1,2\*</sup>

**We have measured the shear forces between solid surfaces sliding past each other across aqueous salt solutions, at pressures and concentrations typical of naturally occurring systems. In such systems the surface-attached hydration layers keep the compressed surfaces apart as a result of strongly repulsive hydration forces. We find, however, that the bound water molecules retain a shear fluidity characteristic of the bulk liquid, even when compressed down to films  $1.0 \pm 0.3$  nanometer thick. We attribute this to the ready exchange (as opposed to loss) of water molecules within the hydration layers as they rub past each other under strong compression.**

The presence of water molecules tightly bound to ions or ionized surfaces in aqueous electrolytes leads to strong repulsion when they approach each other to within a few nanometers or less (1–4). This effect is thought to arise from the reluctance of the ions or surfaces to shed their hydration sheath (3–6). It can dominate the double-layer repulsion/van der Waals attraction mechanisms [accounted for in the classic DLVO (Derjaguin, Landau, Verwey, and Overbeek) theory (7)] and is particularly important at the high salt concentrations ( $\sim 0.1$  M salt) found in nature. The way in which the properties of such hydration layers differ from those of bulk water has for decades excited much debate (8–11). At issue here is a simple question: Is the hydration layer surrounding such highly confined bound ions fluid, or is it highly viscous? The difference is crucial and is directly implicated in areas ranging from clay plasticity (12) and biolubrication (13) to gating of charge migration in DNA (14). In addition, many biological processes require shear and displacement of the final subnanometer layers of bound hydration layers before molecular contact or passage. These include interactions between ligands and receptors, transport within the very crowded

intracellular environment (15) or through ion channels (16), and protein folding (17).

Extensive direct measurements, as well as modeling (1–4, 6), have shed much light on equilibrium interactions of such bound hydration layers. In contrast, few direct measurements have been reported concerning their fluidity (18–22), particularly in the regime of the hydration sheaths, i.e., films of thickness  $D = 7$  to  $10 \text{ \AA}$  (23–25). We used a surface force balance (SFB) with extreme sensitivity in measuring shear interactions to probe directly the fluidity of aqueous electrolytes compressed and sheared between molecularly smooth mica surfaces. While our results confirm the long-established equilibrium hydration repulsion, they reveal at the same time that the bound water in the hydration layers remains extremely fluid under shear. This fluidity persists down to films in the range  $D = D_c = 1.0 \pm 0.3 \text{ nm}$ , a thickness comparable to the size of hydrated ions in solution. Within such films, most of the confined water molecules are expected to be in bound hydration layers.

The SFB used has been described in detail (26). Its main features are schematically outlined in Fig. 1. We focus here on investigations of NaCl solutions, although preliminary studies on  $\text{KNO}_3$  solutions (in the hydration repulsion regime) reveal very similar findings. The following results are based on several different experiments (different pairs of mica sheets), as well as on different contact

positions within an experiment. Initial measurements in salt-free water were found to be crucial to establish the integrity and purity of the system. They were made to ensure the removal of any contaminant layers that adsorb on the mica while exposed to air (2, 27, 28), so as to attain true (mica-lattice/mica-lattice) contact between the surfaces (29). When the above behavior (29) could not be reproduced, as in our own earlier studies (30), subsequent measurements at high salt concentrations revealed high effective viscosities already at values of  $D$  as low as  $< 2$  to  $3 \text{ nm}$ , and these were attributed to contamination. A previous observation (31, 32) of comparably high viscosities in salt solutions ( $\sim 0.03 \text{ M}$ ) confined to  $D < 2$  to  $2.5 \text{ nm}$  may have been related to this. Improvements in water purification and handling in the present study resolved this problem, as shown in figure 1 of (33) and in Fig. 1 of this study.

High-purity NaCl was then added to a concentration of  $10^{-3} \text{ M}$  ( $\pm 10\%$ ), and normal and shear forces were measured as a further control. Mica loses  $\text{K}^+$  ions to solution, leaving a net negative surface charge, and the resultant distribution of ions in the intersurface gap leads to a long-ranged osmotic repulsion followed by a jump-in to adhesive mica/mica contact, in close agreement with earlier studies (3, 4) and in accord with DLVO theory (7) (Fig. 1). Such total extrusion of the low-salt electrolyte from between the adhering surfaces resembles that observed in salt-free water (33) and is thought to arise when the predominant hydroxonium  $\text{H}_3\text{O}^+$  ions condense into the charged mica, retaining no hydrated layers at the surface (3, 4).

Shear forces were measured as described recently (33). With the surfaces compressed down to separations of a few nm, the upper mica surface is made to move laterally back and forth, exactly parallel to the lower one at velocity  $v_s$  (Fig. 1 inset, upper trace). The shear forces  $F_s$  transmitted across the intersurface gap are simultaneously recorded as the surfaces further approach under slow thermal drift. No shear forces greater than the noise-limited sensitivity  $\delta F_s$  ( $\pm 30 \text{ nN}$ ) are detected between the surfaces down to adhe-

<sup>1</sup>Weizmann Institute of Science, Rehovot 76100, Israel. <sup>2</sup>Physical and Theoretical Chemistry Laboratory, Oxford University, Oxford OX1 3QZ, UK.

\*To whom correspondence should be addressed.